DR. KONSTANTIN MOMOT (Orcid ID : 0000-0002-5695-153X)

# Transverse relaxation-based assessment of mammographic density and breast tissue composition by single-sided portable NMR

Tonima S Ali[1, 2]

Monique C. Tourell[1, 2]

Honor J Hugo[2, 3, 4]

Chris Pyke[5]

Samuel Yang[6]

Thomas Lloyd[7]

Erik W. Thompson[2, 3, 4, 8]

*Konstantin I. Momot[1, 2]


[1]School of Chemistry, Physics and Mechanical Engineering, Queensland University of Technology (QUT), Brisbane, Australia

[2]Institute of Health and Biomedical Innovation, Queensland University of Technology (QUT), Brisbane, Australia

[3]School of Biomedical Sciences, Faculty of Health, Queensland University of Technology (QUT), Brisbane, Australia

[4] Translational Research Institute, Woolloongabba, Australia

[5]Department of Surgery, Mater Hospital, University of Queensland, St Lucia, Australia

[6]Department of Plastic and Reconstructive Surgery, Greenslopes Private Hospital, Brisbane, Australia

[7]Division of Radiology, Princess Alexandra Hospital, Woolloongabba, Australia

[8]University of Melbourne Department of Surgery, St Vincent's Hospital, Melbourne, Australia


* Corresponding Author:    Dr Konstantin I. Momot

School of Chemistry, Physics and Mechanical Engineering

Queensland University of Technology (QUT)

GPO Box 2434

Brisbane, QLD 4001

Australia

Email: k.momot@qut.edu.au

Word count:    Abstract        250

Main body        5000    (Introduction to Conclusions inclusive)

**Abstract**

**Purpose:** Elevated mammographic density (MD) has been established as an independent risk factor for breast cancer (BC) as well as a source of masking in X-ray mammography. High-frequency longitudinal monitoring of MD could also be beneficial in hormonal BC prevention, where early MD changes herald the treatment's success. We present a novel approach to quantification of MD in breast tissue using single-sided portable NMR. Its development was motivated by the low cost of portable-NMR instrumentation, suitability for measurements *in vivo*, and the absence of ionizing radiation.

**Methods:** Five breast slices were obtained from three patients undergoing prophylactic mastectomy or breast reduction surgery. Carr-Purcell-Meiboom-Gill (CPMG) relaxation curves were measured from: (1) regions of high and low MD (HMD and LMD, respectively) in the full breast slices; (2) the same regions excised from the full slices; and (3) excised samples after $H_2O$-$D_2O$ replacement. $T_2$ distributions were reconstructed from the CPMG decays using Inverse Laplace Transform.

**Results:** Two major peaks, identified as fat and water, were consistently observed in the $T_2$ distributions of HMD regions. LMD $T_2$ distributions were dominated by the fat peak. The relative areas of the two peaks exhibited statistically significant ($P<0.005$) differences between HMD and

LMD regions, enabling their classification as High- or Low-MD. The relative-area distributions exhibited no statistically significant differences between full slices and excised samples.

**Conclusion:** $T_2$-based portable-NMR analysis is a novel approach to MD quantification. The ability to quantify tissue composition, combined with the low cost of instrumentation, make this approach promising for clinical applications.

**Keywords:** Nuclear Magnetic Resonance, single-sided portable NMR, NMR-MOUSE, breast cancer, mammographic density, transverse spin relaxation time constant ($T_2$)

# 1 INTRODUCTION

Mammographic density (MD), also known as breast density, is estimated in clinical practice from X-ray mammograms and serves as an indicator of breast tissue composition. High MD (HMD) is associated with a relatively large proportion of stroma, collagen and epithelial tissue. Conversely, low MD (LMD) is associated with relatively large adipose tissue content.[1-5] Elevated MD has been established, along with family or personal history of breast cancer (BC), age and genetic mutations, as a significant independent risk factor for BC.[6-9] Women in the highest MD quartile, after adjustment for age and body mass index, are 4-6 times more likely to develop BC over lifetime than women in the low-MD group.[10,11] Besides being a significant risk factor for breast cancer, HMD is a masking factor in mammography, often making mammographic detection of BC in dense breasts difficult.[9,12,13]

While mammography remains a universally accepted standard for MD assessment, it has a number of important limitations. First, it is a 2D technique used to visualize a 3D anatomical structure; it therefore suffers from projectional imaging artifacts. The second is its use of ionizing radiation, which limits its suitability for young women and women with inherited syndromes associated with radio-sensitivity and/or cancer risk.[14,15] Importantly, it also limits the clinically acceptable screening frequency (normally no more than once every 2 years). There are scenarios where frequent longitudinal monitoring of MD would be of clinical benefit, e.g. Tamoxifen treatment for BC prevention, where early MD changes are currently the only known biomarker of the eventual success or failure of the treatment.[16,17] All these factors have both encouraged and necessitated the

development of non-ionizing alternatives for breast screening that may measure MD-analogous quantities.

We have recently shown that quantitative $T_1$ measurements using single-sided portable NMR are capable of distinguishing between HMD and LMD regions in excised breast tissue slices.[18] This suggests that portable NMR could potentially complement other non-ionizing techniques measuring breast density-equivalent quantities:[19,20] ultrasound,[21,22] bioimpedance,[23] transillumination[24,25] and MRI.[11,26-29] Magnetic Resonance in general, and portable NMR in particular, appear promising for quantification of MD because of the great signal editing flexibility offered by MR. Multi-sequence clinical MRI followed by automatic segmentation has been used for quantification of fibroglandular breast tissue (FGT) content, with the conclusion that MRI "provides a reproducible assessment of the proportion of FGT, which correlates well with mammographic assessment of breast density [based on Breast Imaging Reporting and Data System (BI-RADS)]".[30] MRI-based volumetric breast density measurements, using semi-automated or fully-automated clustering or segmentation algorithms, have shown good agreement with conventional MD measurements in multiple studies.[26,29,31-35] Portable NMR offers the ability to quantify tissue spin-relaxation and diffusion properties, which have been shown to provide reliable quantification of MD in conventional breast MRI. Portable NMR also has the added advantages of low purchasing and running cost and low maintenance, largely due to the absence of superconducting magnets (which obviates the need for cryogens). Portable-NMR systems, most notably NMR-MOUSE,[36-38] are commercially available and have been used in a number of biomedical applications including testing of silicone breast implants[39] and studies of various biological tissues, including tendon,[40] articular cartilage,[41,42] skin [43,44] and trabecular bone.[45]

In the present study, we follow up on the $T_1$-based portable-NMR quantification of MD reported earlier[18] and explore the capabilities of $T_2$-based portable-NMR analysis for the assessment of MD in human breast tissue. Transverse spin relaxation in biological tissues is sensitive to the chemical composition and microscopic organization of the tissue.[46-56] In ^{1}H NMR of breast tissue, two major sources of the NMR signal are present: water (the principal signal source in FGT) and fat (which dominates in adipose tissue). These two chemical components exhibit significantly different $T_2$ values and can be resolved in $T_2$ relaxation spectra obtained from Inverse Laplace Transforms (ILT) of Carr-Purcell-Meiboom-Gill (CPMG) relaxation decays.[57] In portable NMR, ILT-based $T_2$ analysis has been used in a wide variety of applications, including skin.[43] Outside of portable NMR, MRI-based multi-exponential $T_2$ relaxation analysis has been applied to normal breast,[58] liver[59] and prostate tissues,[60] as well as pathologies of the brain.[61-65] ILT-based relaxometry has also been used to assess water and fat distribution in processed food products.[66]

We demonstrate that, in excised breast tissue samples, the relative area fractions (*AF*) of fat and water peaks in ILT $T_2$ spectra enable discrimination between HMD and LMD regions. To our knowledge,

this is the first time ILT $T_2$ spectra have been used for compositional quantification of soft biological tissues. The key advantage of this approach is that, unlike $T_1$-based measurements,[18] it enables explicit quantification of the Water:Fat ratio in breast tissue. We discuss how this approach could be used for quantification of MD and evaluation of the relative amount of FGT within breast tissue.

## 2    METHODS

### 2.1    Tissue selection and preparation

Patients presenting with ductal carcinoma in-situ and/or micro-calcifications on radiological investigation were excluded from this study. Five breast slices (the same as those used in our previously reported study[18]) were obtained from three women who underwent breast reduction surgery (Patient 1) or prophylactic mastectomy (Patients 2 and 3). Immediately after the surgery, excised tissues were transported on ice to the pathology suits, and cranio-caudal slices of breast tissue were resected in a sterile environment.[1,2,7,67]. The breast slices were assessed for abnormalities by a pathologist. Slices that were surplus to pathologists' needs were used for the present study. For *Patient-1* and *Patient-3*, the slices were transported for mammography fresh (on ice) immediately after accrual. For *Patient-2*, the slice was stored at -80°C long-term and was transported on dry ice for mammography. Further details can be found in Table 1, ref. 18.

The study was approved by Peter MacCallum Human Research Ethics Committee (#08/21), Metro South Hospital and Health Services, Queensland (HREC/16/QPAH/107), Mater Research (RG-16-028-AM02, MR-2016-32), and administratively approved by Queensland University of Technology (QUT) (#1600000261). The study was conducted in accordance with the Australian National Statement on Ethical Conduct in Human Research (2007).

### 2.2    Slice Mammogram Acquisition and Analysis

Mammography of the breast slices (Mo target/Mo filter; tube voltage 28 kV; exposure 40 mAs) was performed at the Radiology suite, Princess Alexandra Hospital (PAH). Mammograms for *Patient-1*, *Patient-2* and *Patient-3* were acquired from fresh, frozen and fresh slices, respectively. In the mammogram of each slice, one HMD and one LMD region were identified by a clinical radiologist (TL). Following mammography, all slices were kept frozen (–80°C) and later transferred to a freezer (–20°C) at QUT's Gardens Point campus, where they were kept until the portable-NMR measurements. The use of frozen samples is consistent with the previously established experimental protocol;[18] Supporting Information Figure S1 illustrates the absence of significant effects of freezing on the spatial distribution of mammographic density of the samples.

JPEG images of the mammograms of the three slices of *Patient-1* were read in MATLAB R2014a (MathWorks, Natick, MA, USA). Rectangular ROIs, approximately the same size as the portable-NMR sensing coil, were identified in the HMD and the LMD regions of the slices. Greyscale pixel values of the ROIs were used to construct histograms for further analysis, which was performed using an in-house MATLAB code.

## 2.3  Portable-NMR Measurements

The breast slices were defrosted prior to the NMR measurements and kept at room temperature during the measurements. Portable-NMR measurements were performed using a PM5 NMR-MOUSE® instrument (Magritek, New Zealand). This instrument is a single-sided NMR scanner that uses an assembly of permanent magnets to create a horizontal magnetic field $B_0$ = 0.47 T and a vertical permanent field gradient $G_0$ = 22.5 T/m. It uses a surface coil for excitation and signal detection. The instrument enabled the selection of a horizontal sensing slice with an approximate sensing area of 15 x 15 mm (determined by the dimensions of the surface coil) and 50 μm thickness (determined by the amplitude of the magnetic field gradient, RF field strength and the acquisition dwell time). The NMR-MOUSE setup and sample placement are described in detail in our previous work.[18] All $T_2$ relaxation curves were obtained using the CPMG pulse sequence (*TE* = 120 μs, *TR* = 10 s, 4000 integrated echoes and 64 averages, scan time was 11 minutes per scan).

One HMD and one LMD region were identified in each breast slice by visual comparison of the topography of the physical slice with the slice mammogram, where HMD and LMD regions had previously been marked (section 2.2). Three sets of $T_2$ relaxation data were acquired from each slice. First, the HMD and LMD regions were measured within the full slice: the slice was placed such that the required region was located above the center of the NMR-MOUSE sensing coil.[18] A depth profile of the region was acquired in order to check the uniformity of the sample. CPMG decays were acquired at the depths of 2 mm and 4 mm for the four samples that were ~10 mm thick (*Patient1-Slice1*, *Patient1-Slice2*, *Patient1-Slice3* and *Patient3-Slice1*). A single CPMG decay was acquired at the 2 mm depth for the thinner sample (*Patient2-Slice1*, ~4 mm thick).

The second set of CPMG data was obtained from the HMD and LMD regions excised from the respective slices. The regions (smaller than the sensing area of the NMR-MOUSE) were excised using sterile blades in a Physical Containment level 2 (PC2) laboratory. CPMG decays were acquired for all excised HMD and LMD regions using the same protocol as used for the full-slice measurements.

The third set of CPMG data was obtained from the excised regions subjected to $H_2O$–$D_2O$ replacement. The excised samples were soaked in 0.01 M phosphate buffered saline (PBS) solution made with 99% $D_2O$ for 16-18 hours at +4°C, after which portable-NMR measurements were

repeated again using the same protocol. The full dataset, therefore, comprised 54 CPMG decay curves: three curves (full slice, excised, and excised after $H_2O$–$D_2O$ replacement) from each of the 9 different HMD and 9 different LMD locations (two depths each in 4 of the slices and a single depth in the fifth slice, see above). Data acquisition was completed over three days, with the samples being alternated between room temperature (when being measured) and +4°C (between measurements). Two control samples (excised from *Patient1-Slice1*) were subjected to the same experimental protocol over the same time period in order to check for signs of tissue degradation (as seen in $T_2$ relaxation measurements).

## 2.4 $T_2$ Relaxation Analysis

The $T_2$ relaxation curves were analyzed using one-dimensional ILT.[68] The time-dependent signal describing a multicomponent $T_2$ relaxation decay can be written as

$$S(t_j) = g_j = \sum_{i=1}^{m} A(T_i)\exp\left(-\frac{t_j}{T_i}\right) + \varepsilon_j \tag{2}$$

where $i = 1...m$ (the number of relaxation-time components); $T_i$ are the respective relaxation time constants; $A(T_i)$ are the (non-negative) relative amplitudes of the relaxation-time components; $\varepsilon$ is the noise; and $j = 1...n$ (the number of sampled echoes). The amplitudes $A(T_i)$ can in principle be determined by inverting the $T_2$ relaxation curve using a non-negative least-squares algorithm that minimizes the $\chi^2$ value:[69]

$$\min\left\{\chi^2 = \sum_{j=1}^{n}\left(g_j - \sum_{i=1}^{m} A(T_i)\exp\left(-\frac{t_j}{T_i}\right)\right)^2\right\} \tag{3}$$

A robust fit in presence of noise requires a regularization function weighted by a regularization parameter $\alpha$.[70-73] The new minimization function takes the form[68]

$$\min\left\{\chi^2 = \sum_{j=1}^{n}\left(g_j - \sum_{i=1}^{m} A(T_i)\exp\left(-\frac{t_j}{T_i}\right)\right)^2 + \frac{1}{\alpha}\sum_{i=1}^{m}\left(2A(T_i) - A(T_{i-1}) - A(T_{i+1})\right)^2\right\} \tag{4}$$

The values $n = 4000$ (the number of echoes) and $m = 100$ (the number of $T_2$ bins) were used. A code originally designed by Venkataramanan *et al.* and subsequently modified was used for solving Eq. [3][68,74] on MATLAB platform. The code can be obtained from Magritek (support@magritek.com). In order to determine the appropriate value of the regularization parameter $\alpha$ for each $T_2$ relaxation curve, a wide range of $\alpha$ ($\sim10^6 - \sim10^{12}$) was specified, and $\chi^2$ calculated at 20 values of $\alpha$ covering

this range. Supporting Information Figure S2 illustrates the effect of the regularization parameter $\alpha$ on ILT spectra. The curve of $\chi^2$ vs $\alpha$ (see Figure S2(A)) was then plotted. The "best" value of $\alpha$ (corresponding to the best trade-off between over-smoothing and an ill-posed inversion) was selected after visual inspection as the point of the apparent maximum of the second derivative (the "L-bend") of this curve. This value was used for the subsequent inversion of the respective CPMG curve. The correct choice of $\alpha$ ensured that the resulting $T_2$ distribution was insensitive to noise while correctly reproducing the different relaxation components contributing to the CPMG decay curve. No obvious L-bend point was observed for the HMD full-slice measurement *Patient2-Slice1-Depth1*. This $T_2$ distribution was not included in the analysis of the results. However, for a complete understanding of the data used in this study, it was included in the Supporting Information.

The resulting $T_2$ distributions were plotted in semilog coordinates (signal amplitude vs $\log T_2$). They typically exhibited distinct peaks, which were interpreted as arising from either water or fat, as described in Results. Area fraction (*AF*) and geometric-mean $T_2$ (*$gmT_2$*), two measures commonly used for assessing such distributions,[65,66,75-80] were used to characterize the peaks:

$$AF = \frac{\sum_{T_{2min}}^{T_{2max}} A(T_2)}{\sum A(T_2)} \quad [4]$$

$$gmT_2 = exp\left(\frac{\sum_{T_{2min}}^{T_{2max}} A(T_2)\, logT_2}{\sum_{T_{2min}}^{T_{2max}} A(T_2)}\right) \quad [5]$$

where $T_{2min}$ and $T_{2max}$ are the left and right boundaries of the respective peak. Welch's unequal variances t-test was used to evaluate the statistical significance of the difference between the groups of *$gmT_2$* and *AF* values corresponding to HMD and LMD regions; water and fat peaks; and measurements made from full slices versus excised samples.

# 3    RESULTS

The photograph and the mammogram of a representative breast tissue slice (*Patient1-Slice2*) are shown in Figure 1. The ROIs (dashed rectangles in Figure 1(A)) were selected to correspond in size and shape to the sensing area of the RF surface coil of the NMR-MOUSE. Rectangular HMD and LMD ROIs were chosen in this way for each breast slice.

The three slice mammograms obtained from *Patient-1* slices were analyzed to identify the 8-bit greyscale values associated with the HMD and LMD regions. Figure 2 presents the histograms

obtained from the HMD and LMD regions of the three *Patient-1* slice mammograms, with the mammogram pixel values quantified using the 0-255 range (0 is "black" and 255 "white"). The histograms derived from the HMD regions had higher greyscale values than those from LMD regions. However, the HMD and LMD histograms exhibited an overlap, which in some cases was significant.

Figure 3A shows representative $T_2$ distributions measured from an excised HMD region (as shown in Figure 1) before and after $H_2O$-$D_2O$ replacement. $D_2O$ is "silent" in ^{1}H NMR, and therefore the $T_2$ values in distribution *a* (shown in orange) can be interpreted as those of fat. The $T_2$ distribution *b* (shown in blue) was obtained from the native ($H_2O$-containing) tissue; the $T_2$ modes in this distribution can be interpreted as tissue fat ($T_2 \sim 90$ ms) and water ($T_2 \sim 10$ ms). Figure 3B shows the equivalent $T_2$ distributions measured from an excised LMD region (see Figure 1). There, the $T_2$ values of distribution *a* (in purple, measured from the $D_2O$-replaced sample) can be interpreted as the fat component of the LMD sample. The $T_2$ distribution of the native $H_2O$-containing tissue (distribution *b*, in green) had two well-separated modes. The dominant mode (84.99% of the signal, $T_2 \sim 90$ ms) can be interpreted as tissue fat, while the smaller mode at $T_2 \sim 10$ ms can be interpreted as tissue water. Figure 4 shows the $T_2$ distributions measured from all excised HMD and LMD samples used in this study both before and after the $H_2O$-$D_2O$ replacement. The *AF* and *gmT₂* values measured from these distributions are summarized in Supporting Information Tables S1 and S2.

Figure 5A shows a representative $T_2$ distribution measured from a HMD region of a full slice (distribution *f*, shown in light-blue) as well as the $T_2$ distribution measured from the same HMD region after its excision (distribution *e*, in brown). The "fat" and "water" peaks are evident in both $T_2$ distributions. The corresponding peaks in each distribution exhibit approximately equal most-probable $T_2$ values, while the relative amplitudes and the *AF* values (see Supporting Information Tables S1 and S3) of these peaks differed between the two distributions. Figure 5B shows the equivalent two $T_2$ distributions measured from a LMD region of the same slice (distribution *f*, light-green, within the full slice; distribution *e*, magenta, from the excised LMD region). Both peaks are again evident and exhibit approximately equal most-probable $T_2$ values in the two distributions (see Supporting Information Tables S2 and S3). Figure 6 shows the $T_2$ distributions obtained from all HMD and LMD regions within the full slices. The *AF* and *gmT₂* values measured from these distributions are presented in Supporting Information Table S3.

In order to check the compositional stability of the tissue over the course of the measurements, $T_2$ distributions were measured from two control samples, CTRL1 and CTRL2, on three consecutive days. In the CTRL1 sample, the "fat" peak had the most-probable $T_2$ 81.10 ms, 88.92 ms and 81.10 ms; gm$T_2$ 80.11 ms, 76.70 ms and 79.27 ms; and *AF* 81.80%, 85.62% and 80.17% in days 1, 2, and 3, respectively. The "water" peak had the most-probable $T_2$ 9.54 ms, 7.92 ms and 9.54 ms; gm$T_2$ 10.18 ms, 7.55 ms and 10.26 ms; and *AF* 17.87%, 14.37% and 19.35% at the same time points. (The sum of

water and fat AF values was <100% because the area of the entire $T_2$ distribution was taken as 100%.) The corresponding values in the CTRL2 sample were: "fat" peak, most-probable $T_2$ 81.10, 88.92 and 81.10 ms; gm$T_2$ = 76.41, 77.61 and 79.71 ms; $AF$ = 93.15%, 91.42% and 87.28%; "water" peak, most-probable $T_2$ = 9.54, 7.92 and 11.50 ms; gm$T_2$ = 10.98, 8.51 ms and 11.39 ms; $AF$ = 6.83%, 8.54% and 11.71%. These results indicate that there was no statistically significant change in the most-probable $T_2$, gm$T_2$ or $AF$ values during the measurement cycle that could be attributed to sample degradation. This result is in agreement with our $T_1$ study, where $T_1$ values were found to be consistent throughout the three days of the measurement.[18]

As a visual summary of the $T_2$-based analysis, the $AF$ values of the $T_2$ peaks were plotted against the respective gm$T_2$ values for the four groups of measurements: excised HMD regions, excised LMD regions, HMD regions within the full slice, and LMD regions within the full slice. The results are shown in Figures 7A and 7B for the excised and full-slice samples, respectively. Figure 7 shows the large difference between the $T_2$'s of the "fat" and "water" peaks, which can be clearly distinguished based on their gm$T_2$ values. Table 1 shows the results of Welch's t-test for the gm$T_2$ values; these demonstrate that the gm$T_2$ distributions of water peaks were significantly different from those of the fat peaks in all samples. There were no statistically significant differences between the gm$T_2$ distributions of either water or fat peaks between the HMD and LMD regions in either group of samples. Table 2 shows that the distributions of the $AF$ values measured from HMD regions were significantly different from those of the LMD regions, both for excised samples and full-slice samples. There were no statistically significant differences between the $AF$ (Table 2) or gm$T_2$ (Table 1) measurements between full-slice and excised samples.

**DISCUSSION**

The radiographic appearance of the breast is determined by the ratio of FGT and adipose tissue: HMD regions are known to contain a larger proportion of FGT than LMD regions.[9,81-83] The effective transverse spin-relaxation time constants ($T_{2eff}$) of water and fat are determined by the relative amounts of the intracellular and extracellular water, as well as the association of extracellular water with the biopolymers of the extracellular matrix.[81-83] The $T_{2eff}$ values measured under portable-NMR conditions are further dependent upon the diffusion properties of water and fat:[43,84]

$$\frac{1}{T_{2eff}} = \frac{1}{T_2} + \frac{D\,\gamma^2 G_0^2}{12}TE^2 \qquad [6]$$

where $D$ is the diffusion coefficient of the relevant chemical species and $G_0$ is the magnetic field gradient strength. The time constant $T_{2eff}$ is therefore a composite function of the true intrinsic $T_2$ and

diffusion properties of the relevant chemical species. In this study we analyzed how the ILT-derived distributions of $T_{2eff}$ values could be used as "signatures" of HMD and LMD regions of breast tissue samples.

Slice mammograms provide a "gold-standard" reference for identification of HMD and LMD regions within the breast slices. Figure 2 illustrates that, in mammograms, FGT-rich HMD regions tend to exhibit higher X-ray attenuation coefficient and consequently higher image intensity than (adipose-rich) LMD regions.[9] Overlaps between the HMD and LMD distributions suggest that a given ROI may contain both FGT and adipose tissue. This is consistent with the observed distributions of $T_{2eff}$, which demonstrate the coexistence of water and fat in all HMD and LMD regions measured. The nomenclature "HMD region" or "LMD region" is therefore used here to indicate the preponderance of a given tissue type in the ROI, rather than an exclusive presence of FGT or adipose tissue in that region.

Another feature evident in Figure 2 is that the histograms obtained from LMD regions were more homogeneous than those of HMD regions. This observation is also in agreement with the $T_{2eff}$ distributions, which show that the contribution of water to the NMR signal was very low in all LMD regions (significantly lower than the signal contribution from fat in the HMD regions).

The $H_2O$-$D_2O$ replacement measurements enabled identification of the two principal peaks in $T_2$ distributions as water ($T_2 \sim 10$ ms) and fat ($T_2 \sim 80$ ms). Figures 4 and 6 and Table 1 show that there was no significant difference in the $T_2$ values of either water or fat peaks between HMD and LMD regions. This suggests that the microenvironments experienced by both water and fat molecules are similar in HMD and LMD regions, which in turn suggests that the mixing of FGT and adipose tissue occurs on a macroscopic length scale.

Fat was identified as the dominant tissue constituent in the LMD regions, with the fat peak consistently having the area fraction >75% in the LMD $T_2$ distributions (Figures 3B, 4C, 5B and 6B; Supporting Information Tables S2 and S3). Fat was also a major tissue constituent in the HMD regions. The relative amplitudes of water peaks were higher in HMD than in LMD regions but exhibited significant variability (HMD water $AF$ between 22.42% and 65.71%, Figures 3A, 4A, 5A, 6A and Supporting Information Tables S1, S2). Nevertheless, the distributions of the $AF$ values of water and fat peaks were significantly different between the HMD and LMD regions both in excised and full-slice samples (Table 2). We therefore conclude that the relative amounts of tissue fat and water measured from $T_2$ distributions can be used to distinguish between HMD and LMD regions.

The ultimate aim of this research is to adapt the portable-NMR methodology for characterization of MD in the full breast *in vivo*. There, the presence of intertwined FGT and adipose tissue domains can

potentially lead to the partial-volume effect and affect the $T_2$ distributions measured. In order to assess the significance of the partial-volume effect, we have measured $T_2$ distributions from the same ROIs within the full slice and after the ROIs were excised (Figures 4, 6 and 7). The $T_2$ distributions measured from full-slice HMD regions exhibited water and fat peaks of comparable amplitudes (Figure 6A). The $T_2$ distributions measured from full-slice LMD regions were dominated by fat peaks, with minor water peaks (Figure 6B). A comparison of $T_2$ distributions acquired from the same tissue regions before and after excision can be seen in Figure 5; this Figure demonstrates that excision can affect the apparent fat:water ratio measured from $T_2$ distributions. However, application of the Welch's t-test to the respective distributions shows that, both for HMD and LMD regions, there was no significant statistical difference between the $AF$ values measured from the full slices and from the excised samples (Table 2).

Figure 7 presents a visual summary of the ability of $T_2$-based portable-NMR analysis to discriminate between High- and Low-MD regions. This Figure demonstrates that water and fat peaks were readily distinguishable based on their $gmT_2$ values. The $gmT_2$ values of both water and fat peaks were similar between all groups of samples (excised and full-slice, HMD and LMD). The HMD regions could be reliably discriminated from LMD based on their relative fat and water content, which is presented in Figure 7 as the respective $AF$ values. The HMD water peaks had significantly higher $AF$ values than LMD water peaks, both in excised and full-slice samples. It can also be seen that the water/fat ratio can vary substantially from one HMD region to another, which is consistent with the wide variation of MD patterns observed in patients.[12,13,85] To re-cap the key findings of this study: 1) the spin-relaxation properties of both fat and water are equivalent between HMD and LMD regions, suggesting that the physical microenvironments of both FGT and adipose tissue are identical between HMD and LMD; 2) the $AF$ values of fat and water peaks are reliable markers for distinguishing between HMD and LMD regions of breast tissue; and 3) the distributions of fat and water $AF$ values were statistically equivalent between full-slice and excised regions, which augurs well for application of the present MD analysis *in vivo*.

We hypothesize that the approach illustrated by Figure 7 can enable classification of breast tissue samples with unknown MD into HMD and LMD groups. To provide comprehensive coverage, we propose that Figure 7 should be extended to include a large number of HMD and LMD regions acquired from patients across the full range of BI-RADS scores (from 1 to 4). A "library" of $T_2$ characteristics for each BI-RADS category may enable a more refined and targeted HMD/LMD classification.

Our previous work has shown that $T_1$-based portable-NMR analysis enables discrimination between HMD and LMD breast tissue.[18] The results of the present study demonstrate $T_1$- and $T_2$-based portable-NMR analyses are potentially complementary MD assessment tools. In particular, the $T_2$-

based analysis presented here provides explicit information about tissue water and fat content, which may be beneficial for understanding the physiological basis of MD.

*Limitations and Future Work*

ILT, which was used to reconstruct the $T_2$ distributions of breast tissue samples, is well-known to be an ill-posed numerical problem that requires regularization of noisy data.[71-74] The regularization parameter ($\alpha$) in this work was selected visually, based on the identification of the L-bend in the $\chi^2$ vs $\alpha$ curve (see Methods). The L-bend was not always unambiguously identifiable, which leaves the possibility of the reconstructed $T_2$ distributions being either over- or under-smoothed. Examination of the most-probable $T_2$ and $gmT_2$ values given in Supporting Information Tables S1 – S3 suggests that there could have been some measurements where the performance of ILT was sub-optimal. For example, the $T_2$ values of the fat peak in excised HMD sample *P3-S1* differ significantly between native and $D_2O$-replaced tissue. This is contrary to the expectation that the fat chemical environment should be unaffected by $H_2O$-$D_2O$ replacement, and such large differences not observed for the majority of the samples. We hypothesize that the origin of these differences lies in the performance of the ILT procedure. Further investigation of the performance of ILT in breast tissue is warranted.

The sample size used (5 breast slices from 3 different patients) is another potential limitation of the present study. This limitation is alleviated by the fact that the ROIs were measured in both the full slices and excised samples, and in most samples the measurements were performed at two different depths. This provided a total of 18 HMD and 18 LMD measurements, which increased the robustness of the statistics. The *p* values reported in Tables 1 and 2, as well as the very good separation of HMD and LMD points in Figure 7, suggest a high degree of confidence that the present analysis reliably distinguishes between HMD and LMD tissue. This is consistent with our earlier $T_1$-based study,[18] which used exactly the same set of physical samples. Nevertheless, further studies with a larger sample size would be beneficial. Furthermore, studies of the temperature dependence of breast tissue $T_2$'s under portable-NMR conditions would benefit the understanding of how the present results might transfer to measurements performed *in vivo* at physiological temperature.

Unlike MRI, portable NMR is a volume-selective spectroscopic rather than a true imaging technique. This imposes restrictions on how much of the breast volume could be covered in a single measurement *in vivo*. Approaches to addressing this issue were discussed in our previous work.[18] Penetration depth of portable-NMR sensors is another potential limitation *in vivo*. This issue can be mitigated by the selection of instrumentation models: e.g., the commercially available NMR-MOUSE model PM25 offers the penetration depth of 25 mm (as opposed to 5 mm by the PM5 model used here); we hypothesize that the former should be sufficient for MD sensing in the majority of clinical scenarios. Furthermore, the instrumentation used in the present study offered a limited thickness of

the sensing slice (50 μm). Although all the samples displayed good agreement between measurements taken at different depths, it is conceivable that in some situations measurements could be sensitive to the precise positioning of the sensor. Alternative designs of portable-NMR instrumentation may be able to alleviate both these issues by enabling a larger sensing volume.[86-91]

Finally, transferability of these results to measurements *in vivo* could be affected by motional artifacts resulting from patient movement and blood flow. Development of portable NMR-specific motion-compensated acquisition schemes[92] will be able to address this issue and provide robust acquisition approaches suitable for clinical measurements.

**CONCLUSIONS**

Portable-NMR $T_2$-based analysis can unambiguously identify HMD and LMD regions in slices of human breast tissue. Importantly, it also provides information about the relative quantities of fat and water within the respective regions, which represents a unique and novel way of assessing breast tissue composition. In both excised and full-slice samples, HMD regions were found to contain higher proportions of water than LMD regions. This is consistent with the relatively high FGT and low adipose tissue content in HMD tissue. Our analysis is in agreement with the identification of HMD and LMD breast tissue regions based on conventional slice X-ray mammograms, as well as the $T_1$-based portable-NMR analysis reported earlier. $T_2$-based portable-NMR analysis has the potential as an informative, cost-effective and safe alternative suitable for high-frequency monitoring of MD. We envisage that it will have clinical utility in breast density screening, as well as predicting the efficacy of hormonal treatments for breast cancer prevention.

## REFERENCES

1.  Huo CW, Chew G, Hill P, Huang D, Ingman W, Hodson L, Brown KA, Magenau A, Allam AH, McGhee E, Timpson P, Henderson MA, Thompson EW, Britt K. High mammographic density is associated with an increase in stromal collagen and immune cells within the mammary epithelium. *Breast Cancer Research: BCR*. 2015;17(1):79.

2.  Lin SJ, Cawson J, Hill P, Haviv I, Jenkins M, Hopper JL, Southey MC, Campbell IG, Thompson EW. Image-guided sampling reveals increased stroma and lower glandular complexity in mammographically dense breast tissue. *Breast Cancer Research and Treatment*. 2011;128(2):505-516.

3.  Huo CW, Chew GL, Britt KL, Ingman WV, Henderson MA, Hopper JL, Thompson EW. Mammographic density—a review on the current understanding of its association with breast cancer. *Breast Cancer Research and Treatment*. 2014;144(3):479-502.

4.  Mirette H, Caroline D. Is Mammographic Density a Biomarker to Study the Molecular Causes of Breast Cancer? In: Uchiyama N, editor. Mammography - Recent Advances: INTECH Open Access Publisher; 2012.

5.  Britt K, Ingman W, Huo C, Chew G, Thompson E. The Pathobiology of Mammographic Density. *Journal of Cancer Biology and Research*. 2014;2(1):1021.

6.  Boyd NF, Guo H, Martin LJ, Sun L, Stone J, Fishell E, Jong RA, Hislop G, Chiarelli A, Minkin S, Yaffe MJ. Mammographic Density and the Risk and Detection of Breast Cancer. *New England Journal of Medicine*. 2007;356(3):227-236.

7.  Huo CW, Waltham M, Khoo C, Fox SB, Hill P, Chen S, Chew GL, Price JT, Nguyen CH, Williams ED, Henderson M, Thompson EW, Britt KL. Mammographically dense

human breast tissue stimulates MCF10DCIS.com progression to invasive lesions and metastasis. *Breast Cancer Research: BCR*. 2016;18:106.

8.    Wolfe JN. Breast patterns as an index of risk for developing breast cancer. *American Journal of Roentgenology*. 1976;126(6):1130-1137.

9.    Yaffe MJ. Mammographic density. Measurement of mammographic density. *Breast Cancer Research: BCR*. 2008;10(3):209-209.

10.   Yaghjyan L, Colditz GA, Collins LC, Schnitt SJ, Rosner B, Vachon C, Tamimi RM. Mammographic breast density and subsequent risk of breast cancer in postmenopausal women according to tumor characteristics. *J Natl Cancer Inst*. 2011;103(15):1179-1189.

11.   McCormack VA, dos Santos Silva I. Breast Density and Parenchymal Patterns as Markers of Breast Cancer Risk: A Meta-analysis. *Cancer Epidemiology, Biomarkers & Prevention*. 2006;15(6):1159.

12.   Carney PA, Miglioretti DL, Yankaskas BC, et al. Individual and combined effects of age, breast density, and hormone replacement therapy use on the accuracy of screening mammography. *Annals of Internal Medicine*. 2003;138(3):168-175.

13.   Buist DSM, Porter PL, Lehman C, Taplin SH, White E. Factors Contributing to Mammography Failure in Women Aged 40–49 Years. *J Natl Cancer Inst*. 2004;96(19):1432-1440.

14.   Bernstein JL, Teraoka SN, John EM, Andrulis IL, Knight JA, Lapinski R, Olson ER, Wolitzer AL, Seminara D, Whittemore AS, Concannon P. The CHEK2*1100delC Allelic Variant and Risk of Breast Cancer: Screening Results from the Breast Cancer Family Registry. *Cancer Epidemiology, Biomarkers & Prevention*. 2006;15(2):348.

15.   Chistiakov DA, Voronova NV, Chistiakov PA. Genetic variations in DNA repair genes, radiosensitivity to cancer and susceptibility to acute tissue reactions in radiotherapy-treated cancer patients. *Acta Oncologica*. 2008;47(5):809-824.

16.     Shawky MS, Ricciardelli C, Lord M, Whitelock J, Ferro V, Britt K, Thompson EW. Proteoglycans: potential agents in mammographic density and the associated breast cancer risk. *Journal of mammary gland biology and neoplasia*. 2015;20(3-4):121-131.

17.     Evans DG, Astley S, Stavrinos P, Harkness E, Donnelly LS, Dawe S, Jacob I, Harvie M, Cuzick J, Brentnall A. Improvement in risk prediction, early detection and prevention of breast cancer in the NHS Breast Screening Programme and family history clinics: a dual cohort study. *NHS National Institute for Health Research Programme Grants for Applied Research*. 2016;4(11):pgfar04110.

18.     Tourell MC, Ali TS, Hugo HJ, Pyke C, Yang S, Lloyd T, Thompson EW, Momot KI. T1-based sensing of mammographic density using single-sided portable NMR. *Magnetic Resonance in Medicine*. 2018;80(3):1243-1251.

19.     Hugo HJ, Tourell MC, O'Gorman PM, Paige AE, Wellard RM, Lloyd T, Momot KI, Thompson EW. Looking beyond the mammogram to assess mammographic density: A narrative review. *Biomed Spectrosc Imaging*. 2018;7(1-2):63-80.

20.     Houssami NL, Sarah J; Ciatto, Stefano. Breast cancer screening: emerging role of new imaging techniques as adjuncts to mammography. *Medical Journal of Australia*. 2009;190(9):493-498.

21.     Blend RR, DF; Kaizer, L; Shannon, P; Tudor-Robers, B; Boyd, NF. Parenchymal patterns of the breast defined by real time ultrasound. *European Journal of Cancer Prevention*. 1995;4(4):293-298.

22.     Glide C, Duric N, Littrup P. Novel approach to evaluating breast density utilizing ultrasound tomography. *Medical Physics*. 2007;34(2):744-753.

23.     Maskarinec G, Morimoto Y, Laguaña MB, Novotny R, Guerrero RTL. Bioimpedence to Assess Breast Density as a Risk Factor for Breast Cancer in Adult Women and Adolescent Girls. *Asian Pacific J Cancer Prev*. 2016;17(1):65-71.

24.     Simick MK, Jong R, Wilson B, Lilge L. Non-ionizing near-infrared radiation transillumination spectroscopy for breast tissue density and assessment of breast cancer risk. *Journal of Biomedical Optics*. 2004;9(4):794-803.

25. Simick MK, Lilge L. Optical transillumination spectroscopy to quantify parenchymal tissue density: an indicator for breast cancer risk. *The British Journal of Radiology*. 2005;78(935):1009-1017.

26. Klifa C, Carballido-Gamio J, Wilmes L, Laprie A, Lobo C, DeMicco E, Watkins M, Shepherd J, Gibbs J, Hylton N. Quantification of breast tissue index from MR data using fuzzy clustering. 2004 1-5 Sept. 2004. p 1667-1670.

27. McDonald ES, Schopp J, Peacock S, Olson ML, DeMartini WB, Rahbar H, Lehman CD, Partridge SC. Diffusion-weighted MRI: Association between patient characteristics and apparent diffusion coefficients of normal breast fibroglandular tissue at 3 tesla. *AJR: Am J Roentgenol*. 2014;202(5):W496-W502.

28. Hawley JR, Kalra P, Mo X, Raterman B, Yee LD, Kolipaka A. Quantification of breast stiffness using MR elastography at 3 Tesla with a soft sternal driver: A reproducibility study. *Journal of Magnetic Resonance Imaging*. 2017;45(5):1379-1384.

29. Khazen M, Warren RML, Boggis CRM, Bryant EC, Reed S, Warsi I, Pointon LJ, Kwan-Lim GE, Thompson D, Eeles R, Easton D, Evans DG, Leach MO. A pilot study of compositional analysis of the breast and estimation of breast mammographic density using 3D T1-weighted MR imaging. *Cancer Epidemiology, Biomarkers & Prevention* 2008;17(9):2268-2274.

30. Petridou E, Kibiro M, Gladwell C, Malcolm P, Toms A, Juette A, Borga M, Dahlqvist Leinhard O, Romu T, Kasmai B, Denton E. Breast fat volume measurement using wide-bore 3 T MRI: comparison of traditional mammographic density evaluation with MRI density measurements using automatic segmentation. *Clinical Radiology*. 2017;72(7):565-572.

31. Klifa C, Carballido-Gamio J, Wilmes L, Laprie A, Shepherd J, Gibbs J, Fan B, Noworolski S, Hylton N. Magnetic resonance imaging for secondary assessment of breast density in a high-risk cohort. *Magn Reson Imaging*. 2010;28(1):8-15.

32. Wei J, Chan H-P, Helvie MA, Roubidoux MA, Sahiner B, Hadjiiski LM, Zhou C, Paquerault S, Chenevert T, Goodsitt MM. Correlation between mammographic

density and volumetric fibroglandular tissue estimated on breast MR images. *Medical Physics*. 2004;31(4):933-942.

33.   Wu S, Weinstein SP, Conant EF, Kontos D. Automated fibroglandular tissue segmentation and volumetric density estimation in breast MRI using an atlas-aided fuzzy C-means method. *Medical Physics*. 2013;40(12):122302.

34.   Nie K, Chen J-H, Chan S, Chau M-KI, Yu HJ, Bahri S, Tseng T, Nalcioglu O, Su M-Y. Development of a quantitative method for analysis of breast density based on three-dimensional breast MRI. *Medical Physics*. 2008;35(12):5253-5262.

35.   Wang J, Azziz A, Fan B, Malkov S, Klifa C, Newitt D, Yitta S, Hylton N, Kerlikowske K, Shepherd JA. Agreement of Mammographic Measures of Volumetric Breast Density to MRI. *PLoS ONE*. 2013;8(12):e81653.

36.   Blümich B, Blümler P, Eidmann G, Guthausen A, Haken R, Schmitz U, Saito K, Zimmer G. The NMR-mouse: construction, excitation, and applications. *Magn Reson Imaging*. 1998;16(5):479-484.

37.   Eidmann GS, R; Blumler, P; BlumichB. The NMR MOUSE, a Mobile Universal Surface Explorer *J Magn Reson A*. 1996;122:104-109.

38.   Casanova F, Perlo J, Blümich B. Single-Sided NMR. In: Casanova F, Perlo J, Blümich B, editors. Single-Sided NMR. Berlin, Heidelberg: Springer Berlin Heidelberg; 2011. p 1-10.

39.   Krüger M, Schwarz A, Blümich B. Investigations of silicone breast implants with the NMR-MOUSE. *Magn Reson Imaging*. 2007;25(2):215-218.

40.   Navon G, Eliav U, Demco DE, Blümich B. Study of order and dynamic processes in tendon by NMR and MRI. *Journal of Magnetic Resonance Imaging*. 2007;25(2):362-380.

41.   Rössler E, Mattea C, Stapf S. Feasibility of high-resolution one-dimensional relaxation imaging at low magnetic field using a single-sided NMR scanner applied to articular cartilage. *J Magn Reson*. 2015;251:43-51.

42. Rössler E, Mattea C, Saarakkala S, Lehenkari P, Finnilä M, Rieppo L, Karhula S, Nieminen MT, Stapf S. Correlations of low-field NMR and variable-field NMR parameters with osteoarthritis in human articular cartilage under load. *NMR Biomed*. 2017;30(8):e3738.

43. Van Landeghem M, Danieli E, Perlo J, Blümich B, Casanova F. Low-gradient single-sided NMR sensor for one-shot profiling of human skin. *J Magn Reson*. 2012;215:74-84.

44. Bergman E, Sarda Y, Ritz N, Sabo E, Navon G, Bergman R, Nevo U. In vivo assessment of aged human skin with a unilateral NMR scanner. *NMR Biomed*. 2015;28(6):656-666.

45. Brizi L, Barbieri M, Baruffaldi F, Bortolotti V, Fersini C, Liu H, Nogueira d'Eurydice M, Obruchkov S, Zong F, Galvosas P, Fantazzini P. Bone volume–to–total volume ratio measured in trabecular bone by single-sided NMR devices. *Magnetic Resonance in Medicine*. 2018;79(1):501-510.

46. Hazlewood CF, Chang DC, Nichols BL, Woessner DE. Nuclear magnetic resonance transverse relaxation times of water protons in skeletal muscle. *Biophys J*. 1974;14(8):583.

47. Fullerton GD, Potter JL, Dornbluth NC. NMR relaxation of protons in tissues and other macromolecular water solutions. *Magn Reson Imaging*. 1982;1(4):209-226.

48. Xia Y, Momot KI, editors. Biophysics and Biochemistry of Cartilage by NMR and MRI: Royal Society of Chemistry; 2016.

49. Momot KI, Pope JM, Wellard RM. Anisotropy of spin relaxation of water protons in cartilage and tendon. *NMR Biomed*. 2010;23(3):313-324.

50. Wellard RM, Ravasio J-P, Guesne S, Bell C, Oloyede A, Tevelen G, Pope JM, Momot KI. Simultaneous Magnetic Resonance Imaging and Consolidation Measurement of Articular Cartilage. *Sensors*. 2014;14(5):7940-7958.

51. Ali TS, Thibbotuwawa N, Gu Y, Momot KI. MRI magic-angle effect in femorotibial cartilages of the red kangaroo. *Magn Reson Imaging*. 2017;43:66-73.

52. Ali TS, Prasadam I, Xiao Y, Momot KI. Progression of Post-Traumatic Osteoarthritis in rat meniscectomy models: Comprehensive monitoring using MRI. *Scientific Reports*. 2018;8(1):6861.

53. Mamisch TC, Trattnig S, Quirbach S, Marlovits S, White LM, Welsch GH. Quantitative T2 mapping of knee cartilage: differentiation of healthy control cartilage and cartilage repair tissue in the knee with unloading - initial results. *Radiology*. 2010;254(3):818-826.

54. Watrin-Pinzano A, Ruaud J-P, Cheli Y, Gonord P, Grossin L, Gillet P, Blum A, Payan E, Olivier P, Guillot G. T2 mapping: an efficient MR quantitative technique to evaluate spontaneous cartilage repair in rat patella1. *Osteoarthr Cartilage*. 2004;12(3):191-200.

55. Hashido T, Saito S. Quantitative T1, T2, and T2* mapping and semi-quantitative neuromelanin-sensitive magnetic resonance imaging of the human midbrain. *PloS one*. 2016;11(10):e0165160.

56. Zia MI, Ghugre NR, Connelly KA, Strauss BH, Sparkes JD, Dick AJ, Wright GA. Characterizing myocardial edema and hemorrhage using quantitative T2 and T2* mapping at multiple time intervals post ST-segment elevation myocardial infarction. *Circulation: Cardiovascular Imaging*. 2012;5(5):566-572.

57. Blümich B, Perlo J, Casanova F. Mobile single-sided NMR. *Progr Nucl Magn Reson Spectrosc*. 2008;52(4):197-269.

58. Graham SJ, Stanchev PL, Bronskill MJ. Criteria for analysis of multicomponent tissue T2 relaxation data. *Magnetic Resonance in Medicine*. 1996;35(3):370-378.

59. Lupu M, Thomas CD, Mispelter J. Retrieving accurate relaxometric information from low signal-to-noise ratio 23Na MRI performed in vivo. *Comptes Rendus Chimie*. 2008;11(4–5):515-523.

60. Storås TH, Gjesdal K-I, Gadmar ØB, Geitung JT, Kløw N-E. Prostate magnetic resonance imaging: Multiexponential T2 decay in prostate tissue. *Journal of Magnetic Resonance Imaging*. 2008;28(5):1166-1172.

61. Laule C, Kozlowski P, Leung E, Li DKB, MacKay AL, Moore GRW. Myelin water imaging of multiple sclerosis at 7 T: Correlations with histopathology. *NeuroImage*. 2008;40(4):1575-1580.

62. Laule C, Vavasour IM, Mädler B, Kolind SH, Sirrs SM, Brief EE, Traboulsee AL, Moore GRW, Li DKB, MacKay AL. MR evidence of long T2 water in pathological white matter. *Journal of Magnetic Resonance Imaging*. 2007;26(4):1117-1121.

63. Sirrs SM, Laule C, Mädler B, Brief EE, Tahir SA, Bishop C, MacKay AL. Normal-appearing White Matter in Patients with Phenylketonuria: Water Content, Myelin Water Fraction, and Metabolite Concentrations. *Radiology*. 2007;242(1):236-243.

64. Schad LR, Brix G, Zuna I, Härle W, Lorenz WJ, Semmler W. Multiexponential proton spin-spin relaxation in MR imaging of human brain tumors. *Journal of computer assisted tomography*. 1989;13(4):577-587.

65. Ali TS, Bjarnason TA, Senger DL, Dunn JF, Joseph JT, Mitchell JR. QuantitativeT2: interactive quantitative T2 MRI witnessed in mouse glioblastoma. *Journal of Medical Imaging*. 2015;2(3):036002.

66. Oztop MH, Bansal H, Takhar P, McCarthy KL, McCarthy MJ. Using multi-slice-multi-echo images with NMR relaxometry to assess water and fat distribution in coated chicken nuggets. *LWT - Food Science and Technology*. 2014;55(2):690-694.

67. Chew GL, Huang D, Lin SJ, Huo C, Blick T, Henderson MA, Hill P, Cawson J, Morrison WA, Campbell IG, Hopper JL, Southey MC, Haviv I, Thompson EW. High and low mammographic density human breast tissues maintain histological differential in murine tissue engineering chambers. *Breast Cancer Research and Treatment*. 2012;135(1):177-187.

68. Venkataramanan L, Yi-Qiao S, Hurlimann MD. Solving Fredholm integrals of the first kind with tensor product structure in 2 and 2.5 dimensions. *IEEE Transactions on Signal Processing*. 2002;50(5):1017-1026.

69. Lawson CA, Hanson R. Solving Least Squares Problems. Englewood Cliffs, NJ: Prentice-Hall; 1974.

70.     Provencher SW. Inverse problems in polymer characterization: Direct analysis of polydispersity with photon correlation spectroscopy. *Die Makromolekulare Chemie*. 1979;180(1):201-209.

71.     Provencher SW. A constrained regularization method for inverting data represented by linear algebraic or integral equations. *Computer Physics Communications*. 1982;27(3):213-227.

72.     Provencher SW. A General-Purpose Constrained Regularization Method for Inverting Photon Correlation Data. In: Schulz-DuBois EO, editor. Photon Correlation Techniques in Fluid Mechanics; 1983; Berlin, Heidelberg. Springer Series in Optical Sciences. p 322-328.

73.     Borgia GC, Brown RJS, Fantazzini P. Uniform-Penalty Inversion of Multiexponential Decay Data. *J Magn Reson*. 1998;132(1):65-77.

74.     Song YQ, Venkataramanan L, Hürlimann MD, Flaum M, Frulla P, Straley C. T1–T2 Correlation Spectra Obtained Using a Fast Two-Dimensional Laplace Inversion. *J Magn Reson*. 2002;154(2):261-268.

75.     Whittall KP, Mackay AL, Graeb DA, Nugent RA, Li DKB, Paty DW. In vivo measurement of T2 distributions and water contents in normal human brain. *Magnetic Resonance in Medicine*. 1997;37(1):34-43.

76.     MacKay A, Laule C, Vavasour I, Bjarnason T, Kolind S, Mädler B. Insights into brain microstructure from the T2 distribution. *Magn Reson Imaging*. 2006;24(4):515-525.

77.     Bjarnason TA, McCreary CR, Dunn JF, Mitchell JR. Quantitative T2 analysis: The effects of noise, regularization, and multivoxel approaches. *Magnetic Resonance in Medicine*. 2010;63(1):212-217.

78.     Laule C, Kolind SH, Bjarnason TA, Li DKB, MacKay AL. In vivo multiecho T2 relaxation measurements using variable TR to decrease scan time. *Magn Reson Imaging*. 2007;25(6):834-839.

79. Whittall KP, MacKay AL, Li DKB, Vavasour IM, Jones CK, Paty DW. Normal-appearing white matter in multiple sclerosis has heterogeneous, diffusely prolonged T2. *Magnetic Resonance in Medicine*. 2002;47(2):403-408.

80. Meyers SM, Vavasour IM, Mädler B, Harris T, Fu E, Li DKB, Traboulsee AL, MacKay AL, Laule C. Multicenter measurements of myelin water fraction and geometric mean T2: Intra- and intersite reproducibility. *Journal of Magnetic Resonance Imaging*. 2013;38(6):1445-1453.

81. Mathur-De Vré R. The NMR studies of water in biological systems. *Progress in Biophysics and Molecular Biology*. 1980;35:103-134.

82. Koenig SH, Brown III RD. Relaxometry of tissue In: Grant DM, Harris RK, editors. Encyclopedia of Nuclear Magnetic Resonance. New York: Wiley; 1996. p 4108-4120.

83. Cameron IL, Ord VA, Fullerton GD. Characterization of proton NMR relaxation times in normal and pathological tissues by correlation with other tissue parameters. *Magn Reson Imaging*. 1984;2(2):97-106.

84. Song YQ. Categories of Coherence Pathways for the CPMG Sequence. *J Magn Reson*. 2002;157(1):82-91.

85. Berg WA, Campassi C, Langenberg P, Sexton MJ. Breast Imaging Reporting and Data System. *American Journal of Roentgenology*. 2000;174(6):1769-1777.

86. Bashyam A, Li M, Cima MJ. Design and experimental validation of Unilateral Linear Halbach magnet arrays for single-sided magnetic resonance. *J Magn Reson*. 2018;292:36-43.

87. Watzlaw J, Gloggler S, Blumich B, Mokwa W, Schnakenberg U. Stacked planar micro coils for single-sided NMR applications. *J Magn Reson*. 2013;230:176-185.

88. Oligschlager D, Lehmkuhl S, Watzlaw J, Benders S, de Boever E, Rehorn C, Vossel M, Schnakenberg U, Blumich B. Miniaturized multi-coil arrays for functional planar imaging with a single-sided NMR sensor. *J Magn Reson*. 2015;254:10-18.

89. Roessler E, Mattea C, Stapf S. Feasibility of high-resolution one-dimensional relaxation imaging at low magnetic field using a single-sided NMR scanner applied to articular cartilage. *J Magn Reson*. 2015;251:43-51.

90. Utsuzawa S, Fukushima E. Unilateral NMR with a barrel magnet. *J Magn Reson*. 2017;282:104-113.

91. Wang Q, Gao R, Liu S. Topology optimization based design of unilateral NMR for generating a remote homogeneous field. *J Magn Reson*. 2017;279:51-59.

92. Momot KI, Kuchel PW. PFG NMR diffusion experiments for complex systems *Concepts Magn Reson*. 2006;28A:249-269.

**Tables**

**Table 1**: Results of Welch's unequal variances t-test between the geometric mean $T_2$ ($gmT_2$) measurements of water peaks and fat peaks that were obtained from the $T_2$ distributions of excised HMD and LMD regions of breast tissue. Shaded cells indicate a statistically significant difference between the respective sample groups ($P < .005$).

| | | | Full Slice | | | | Excised Regions | | | |
|---|---|---|---|---|---|---|---|---|---|---|
| | | | HMD | | LMD | | HMD | | LMD | |
| | | | Water | Fat | Water | Fat | Water | Fat | Water | Fat |
| **Full Slice** | **HMD** | **Water** | | $5.10 \times 10^{-10}$ | 0.25 | $1.89 \times 10^{-8}$ | 0.39 | $1.07 \times 10^{-9}$ | 0.03 | $1.54 \times 10^{-15}$ |
| | | **Fat** | $5.10 \times 10^{-10}$ | | $4.92 \times 10^{-11}$ | 0.29 | $7.95 \times 10^{-11}$ | 0.11 | $5.06 \times 10^{-11}$ | 0.77 |
| | **LMD** | **Water** | 0.25 | $4.92 \times 10^{-11}$ | | $2.66 \times 10^{-9}$ | 0.11 | $1.30 \times 10^{-10}$ | 0.02 | $1.49 \times 10^{-11}$ |
| | | **Fat** | $1.89 \times 10^{-8}$ | 0.29 | $2.66 \times 10^{-9}$ | | $8.05 \times 10^{-9}$ | 0.03 | $7.41 \times 10^{-9}$ | 0.17 |
| **Excised Regions** | **HMD** | **Water** | 0.39 | $7.95 \times 10^{-11}$ | 0.11 | $8.05 \times 10^{-9}$ | | $3.96 \times 10^{-10}$ | 0.18 | $1.93 \times 10^{-17}$ |
| | | **Fat** | $1.07 \times 10^{-9}$ | 0.11 | $1.30 \times 10^{-10}$ | 0.03 | $3.96 \times 10^{-10}$ | | $3.47 \times 10^{-10}$ | 0.18 |
| | **LMD** | **Water** | 0.03 | $5.06 \times 10^{-11}$ | 0.02 | $7.41 \times 10^{-9}$ | 0.18 | $3.47 \times 10^{-10}$ | | $1.50 \times 10^{-17}$ |
| | | **Fat** | $1.54 \times 10^{-15}$ | 0.77 | $1.49 \times 10^{-11}$ | 0.17 | $1.93 \times 10^{-17}$ | 0.18 | $1.50 \times 10^{-17}$ | |

**Table 2**: Results of Welch's unequal variances t-test between the area fraction ($AF$) measurements of water peaks and fat peaks, which were obtained from the $T_{2eff}$ distributions of excised HMD and LMD regions of breast tissue. Shaded cells indicate a statistically significant difference between the respective sample groups ($P < .005$).

| | | Full Slice | | Excised Regions | |
|---|---|---|---|---|---|
| | | HMD | LMD | HMD | LMD |

| | | | Water | Fat | Water | Fat | Water | Fat | Water | Fat |
|---|---|---|---|---|---|---|---|---|---|---|
| **Full Slice** | **HMD** | **Water** | | $9.38 \times 10^{-5}$ | $3.33 \times 10^{-5}$ | $1.02 \times 10^{-8}$ | 0.59 | $2.4 \times 10^{-3}$ | $6.25 \times 10^{-5}$ | $1.23 \times 10^{-7}$ |
| | | **Fat** | $9.38 \times 10^{-5}$ | | $1.33 \times 10^{-7}$ | $8.45 \times 10^{-6}$ | $2.8 \times 10^{-3}$ | 0.61 | $2.02 \times 10^{-7}$ | $1.12 \times 10^{-4}$ |
| | **LMD** | **Water** | $3.33 \times 10^{-5}$ | $1.33 \times 10^{-7}$ | | $4.22 \times 10^{-10}$ | $2.61 \times 10^{-4}$ | $3.69 \times 10^{-6}$ | 0.25 | $1.24 \times 10^{-8}$ |
| | | **Fat** | $1.02 \times 10^{-8}$ | $8.45 \times 10^{-6}$ | $4.22 \times 10^{-10}$ | | $1.82 \times 10^{-6}$ | $7.54 \times 10^{-5}$ | $1.03 \times 10^{-14}$ | 0.01 |
| **Excised Regions** | **HMD** | **Water** | 0.59 | $2.8 \times 10^{-3}$ | $2.61 \times 10^{-4}$ | $1.82 \times 10^{-6}$ | | 0.02 | $5.58 \times 10^{-4}$ | $9.72 \times 10^{-6}$ |
| | | **Fat** | $2.4 \times 10^{-3}$ | 0.61 | $3.69 \times 10^{-6}$ | $7.54 \times 10^{-5}$ | 0.02 | | $7.36 \times 10^{-6}$ | $5.4 \times 10^{-4}$ |
| | **LMD** | **Water** | $6.25 \times 10^{-5}$ | $2.02 \times 10^{-7}$ | 0.25 | $1.03 \times 10^{-14}$ | $5.58 \times 10^{-4}$ | $7.36 \times 10^{-6}$ | | $8.58 \times 10^{-17}$ |
| | | **Fat** | $1.23 \times 10^{-7}$ | $1.12 \times 10^{-4}$ | $1.24 \times 10^{-8}$ | 0.01 | $9.72 \times 10^{-6}$ | $5.4 \times 10^{-4}$ | $8.58 \times 10^{-17}$ | |

**Figure Legends**

**Figure 1**: A photograph (A) and a mammogram (B) of a representative breast slice (*Patient 1-Slice 2*) used in this study. The HMD and LMD regions specified by the radiologist are shown as white circles in (B). The black dashed squares in (A) show the HMD and LMD regions excised from the full slice.

**Figure 2**: Histograms of the intensities of HMD and LMD regions in slice mammograms of *Patient 1-Slice 1* (A), *Patient 1-Sice 2* (B) and *Patient 1-Slice 3* (C). The horizontal axis represents the pixel greyscale values. The vertical axis shows the bin counts, or the abundance, of the respective greyscale values.

**Figure 3**: Representative $T_2$ distributions obtained from excised HMD (A) and LMD (B) breast tissue samples. The samples shown were excised from *Patient 1-Slice 2*. Each panel shows the $T_2$ distribution in the native tissue (labelled "b") and after $H_2O$-$D_2O$ replacement (labelled "a"). The peak near $T_2 = 10$ ms, which disappears upon $H_2O$-$D_2O$ replacement, was identified as water. The measurements shown were taken at the 4 mm tissue depth of the respective samples (Depth 2, P1-S2-D2). In these and all subsequent ILT spectra, the $T_2$ range from 0.1 ms to 1000 ms with logarithmic spacing of bins was used. However, as no $T_2$ contributions were observed for $T_2 < 3$ ms, all ILT $T_2$ distributions were plotted in the range from 1 ms to 1000 ms. The boundaries of the $T_2$ peaks were selected individually for each $T_2$ spectrum, either as the first bin whose value was above the baseline, or as the bin closest to the minimum between the

two peaks. As an example, for spectrum "b" in panel (A) the peak boundaries were defined as 4.98 ms – 22.1 ms for Water and 24.2 ms – 359 ms for Fat. In panel (B), the respective boundaries were defined as 4.13 ms – 13.8 ms and 15.2 ms – 394 ms for spectrum "b" and 20.1 ms – 327 ms for the sole peak in spectrum "a".

**Figure 4**: The $T_2$ distributions obtained from the breast tissue regions excised from the 5 slices used in the study. (A): excised HMD samples before $H_2O$-$D_2O$ replacement; (B): same samples after $H_2O$-$D_2O$ replacement; (C): excised LMD samples before $H_2O$-$D_2O$ replacement; and (D): same samples after $H_2O$-$D_2O$ replacement. The individual distributions represent measurements at a specific depth within a given slice: *Patient 1-Slice 1-Depth 1* (P1-S1-D1), *Patient 1-Slice 1-Depth 2* (P1-S1-D2), *Patient 1-Slice 2-Depth 1* (P1-S2-D1), *Patient 1-Slice 2-Depth 2* (P1-S2-D2), *Patient 1-Slice 3-Depth 1* (P1-S3-D1), *Patient 1-Slice 3-Depth 2* (P1-S3-D2), *Patient 2-Slice 1-Depth 1* (P2-S1-D1), *Patient 3-Slice 1-Depth 1* (P3-S1-D1) and *Patient 3-Slice 1-Depth 2* (P3-S1-D2).

**Figure 5**: The $T_2$ distributions obtained from the full breast slice and from the excised regions of *Patient 1-Slice 2*: (A) HMD region and (B) LMD region. The full-slice measurements were taken with the respective region positioned above the center of the NMR-MOUSE sensing coil. All the measurements shown are from the 2 mm tissue depth (Depth 1, P1-S2-D1).

**Figure 6**: The $T_2$ distributions obtained from the full breast slices used in this study. (A): HMD regions within the full breast slices; and (B): LMD regions within the full slices. The measurements were taken with the respective region positioned above the center of the NMR-MOUSE sensing coil. The individual distributions represent the measurements made at a specific depth within a given slice (see the legend of Figure 4 for the nomenclature).

**Figure 7**: The geometric mean $T_2$ ($gmT_2$) values and the area fractions ($AF$) of the water and fat peaks measured from excised breast tissue samples (A) and the respective regions within the full slices (B). The $gmT_2$ values represent the geometric-average $T_2$ of the water and fat, while the $AF$ values reflect the relative prevalence of the respective chemical species within the sample. This Figure includes the HMD and LMD regions from all five breast tissue slices studied.

**Supporting Information Table Captions**

**Table S1**: The most probable $T_2$ value, $AF$ and $gmT_2$ computed from both water and fat peaks of the $T_2$ distributions measured from excised HMD regions before and after $H_2O$-$D_2O$ replacement. The individual distributions represent measurements at a specific depth within a given slice: *Patient 1-Slice 1-Depth 1* (P1-S1-D1), *Patient 1-Slice 1-Depth 2* (P1-S1-D2), *Patient 1-Slice 2-Depth 1* (P1-S2-D1), *Patient 1-Slice 2-Depth 2* (P1-S2-D2), *Patient 1-Slice 3-Depth 1* (P1-S3-D1), *Patient 1-Slice 3-Depth 2* (P1-S3-D2), *Patient 2-Slice 1-Depth 1* (P2-S1-D1), *Patient 3-Slice 1-Depth 1* (P3-S1-D1) and *Patient 3-Slice 1-Depth 2* (P3-S1-D2). Note that the sum of $AF$(water) and $AF$(fat) is typically slightly lower than 100% because the entire area of each $T_2$ distribution (rather than just the sum of the two peaks) was normalized to 100%.

**Table S2**: The most probable $T_2$ value, *AF* and $gmT_2$ computed from both water and fat peaks of the $T_2$ distributions measured from excised LMD regions before and after $H_2O$-$D_2O$ replacement. The individual distributions represent measurements at a specific depth within a given slice: *Patient 1-Slice 1-Depth 1* (P1-S1-D1), *Patient 1-Slice 1-Depth 2* (P1-S1-D2), *Patient 1-Slice 2-Depth 1* (P1-S2-D1), *Patient 1-Slice 2-Depth 2* (P1-S2-D2), *Patient 1-Slice 3-Depth 1* (P1-S3-D1), *Patient 1-Slice 3-Depth 2* (P1-S3-D2), *Patient 2-Slice 1-Depth 1* (P2-S1-D1), *Patient 3-Slice 1-Depth 1* (P3-S1-D1) and *Patient 3-Slice 1-Depth 2* (P3-S1-D2).

**Table S3**: The most probable $T_2$ value, *AF* and $gmT_2$ computed from both water and fat peaks of the $T_2$ distributions measured from HMD and LMD regions of full-slice samples. The individual distributions represent measurements at a specific depth within a given slice: *Patient 1-Slice 1-Depth 1* (P1-S1-D1), *Patient 1-Slice 1-Depth 2* (P1-S1-D2), *Patient 1-Slice 2-Depth 1* (P1-S2-D1), *Patient 1-Slice 2-Depth 2* (P1-S2-D2), *Patient 1-Slice 3-Depth 1* (P1-S3-D1), *Patient 1-Slice 3-Depth 2* (P1-S3-D2), *Patient 2-Slice 1-Depth 1* (P2-S1-D1), *Patient 3-Slice 1-Depth 1* (P3-S1-D1) and *Patient 3-Slice 1-Depth 2* (P3-S1-D2).

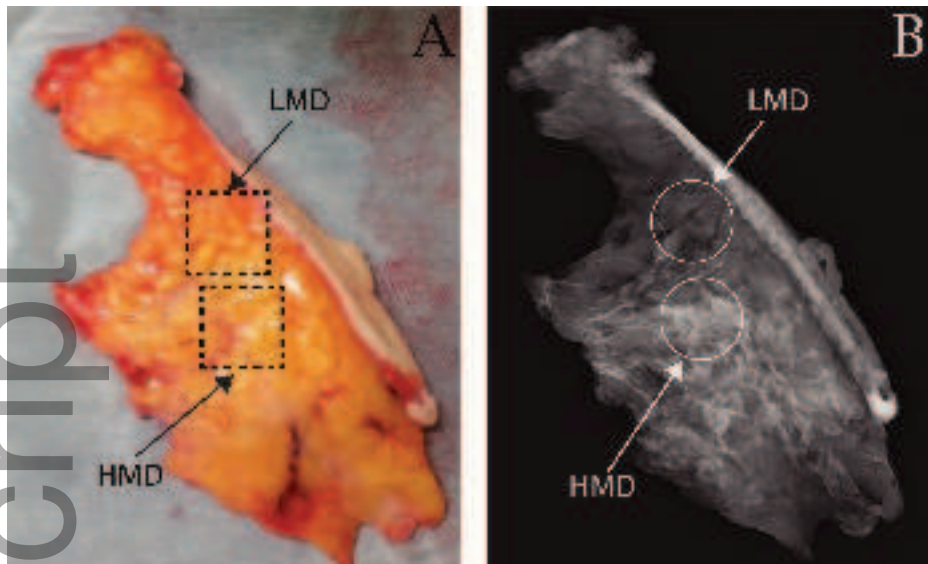**Supporting Information Figure Captions**

**Figure S1**: Comparison of slice mammograms of a (A) fresh and (B) frozen breast tissue slice. The two images are of the same physical slice; image A was obtained from the fresh slice immediately after excision; image B was obtained from the frozen slice following a 1 year 9 months storage at –80 ºC. The slice shown was not used in the main part of this study but is representative of the breast tissue slices used. Freezing-and-thawing cycle causes slight changes in the topography of the sample and local non-uniformity of the sample thickness; any areas thus affected were avoided when selecting the measurement regions. The red circles show the HMD and LMD regions-of-interest (ROIs) selected by the radiologist to match the same topographical features in the fresh and frozen
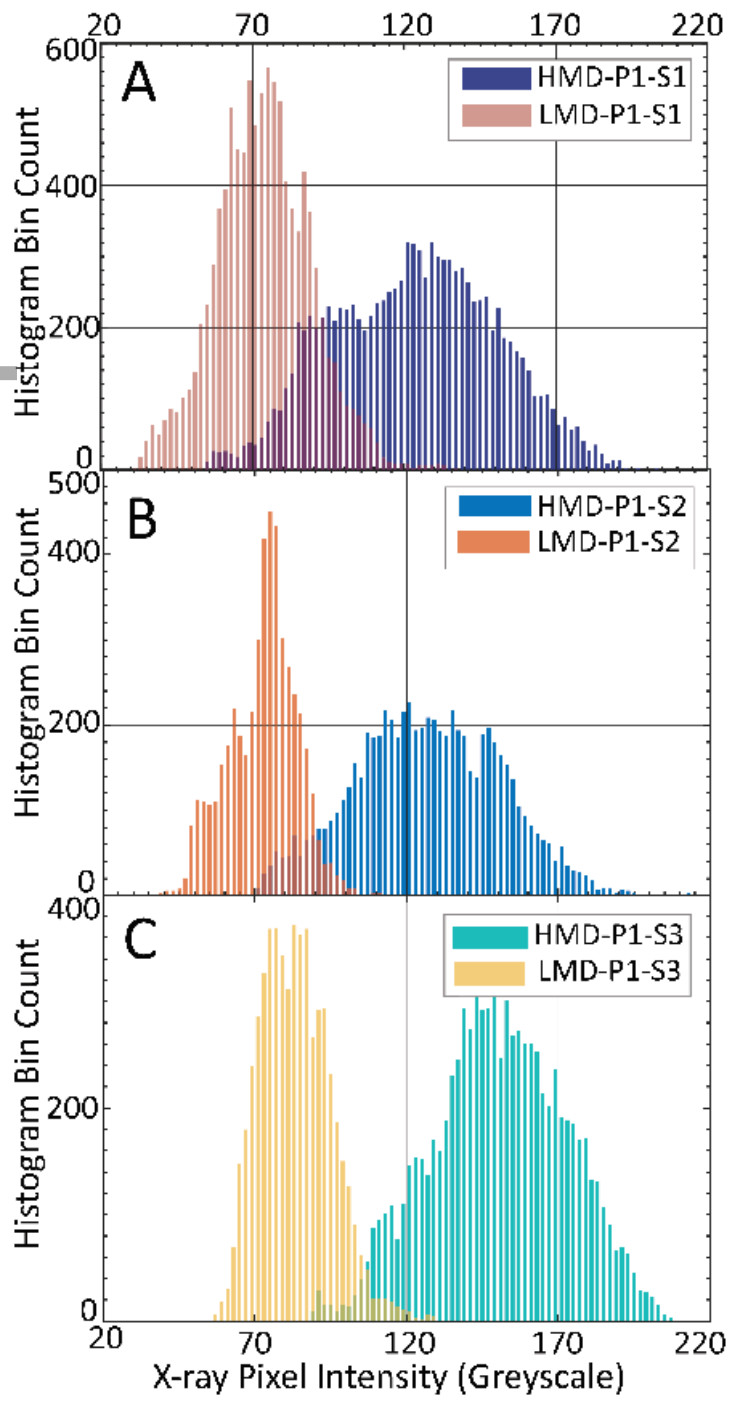
sample. The areas of the ROIs were: (A) 20.4 mm$^2$ (LMD) and 3.8 mm$^2$ (HMD); (B) 13.2 mm$^2$ (LMD) and 7.5 mm$^2$ (HMD). The absorbed dose per unit mass was: (A) 2452 ± 41 Gy (LMD) and 3052 ± 79 Gy (HMD); (B) 2477 ± 76 Gy (LMD) and 3089 ± 137 Gy (HMD). The absorbed doses are similar between the fresh and the frozen sample, indicating that freezing and prolonged storage at –80 $^o$C do not have a significant effect on the distribution of the mammographic density of the sample.

**Figure S2**: Effect of the ILT regularization parameter $\alpha$ on the computed ILT spectra: (A) The main plot is a representative CPMG data set with $n = 4000$ echoes. Each sample point corresponds to one echo integrated from −8 μs to +8 μs from the echo center. The SNR value is 18, which is representative of the remaining data sets. The inset shows the plot of $\chi^2$ *vs* the regularization parameter $\alpha$ for a wide range of $\alpha$ values (see section 2.4 in the main text). This plot is approximately L-shaped. The corner of the "L", which was selected after visual inspection as the point of the apparent maximum of the second derivative of the plot, corresponds to the optimal range of $\alpha$ in the ILT. The circled points labelled b, c and d in the inset correspond to the values of $\alpha$ used to compute the ILT spectra in panels (B), (C) and (D), respectively. (B) An under-regularized ILT spectrum computed with $\alpha$ set too low. This makes the ILT smooth the physical features of the $T_2$ spectrum as well as the noise; the resulting over-smoothed spectrum fails to reliably distinguish between the Fat and Water $T_2$ peaks. (C) A properly regularized ILT spectrum with the $\alpha$ in the optimal range. This spectrum reliably distinguishes between the Fat and Water $T_2$ peaks without introducing spurious peaks. (D) An over-regularized ILT spectrum with the $\alpha$ set too high, making the ILT overly sensitive to noise and resulting in the introduction of spurious $T_2$ peaks.
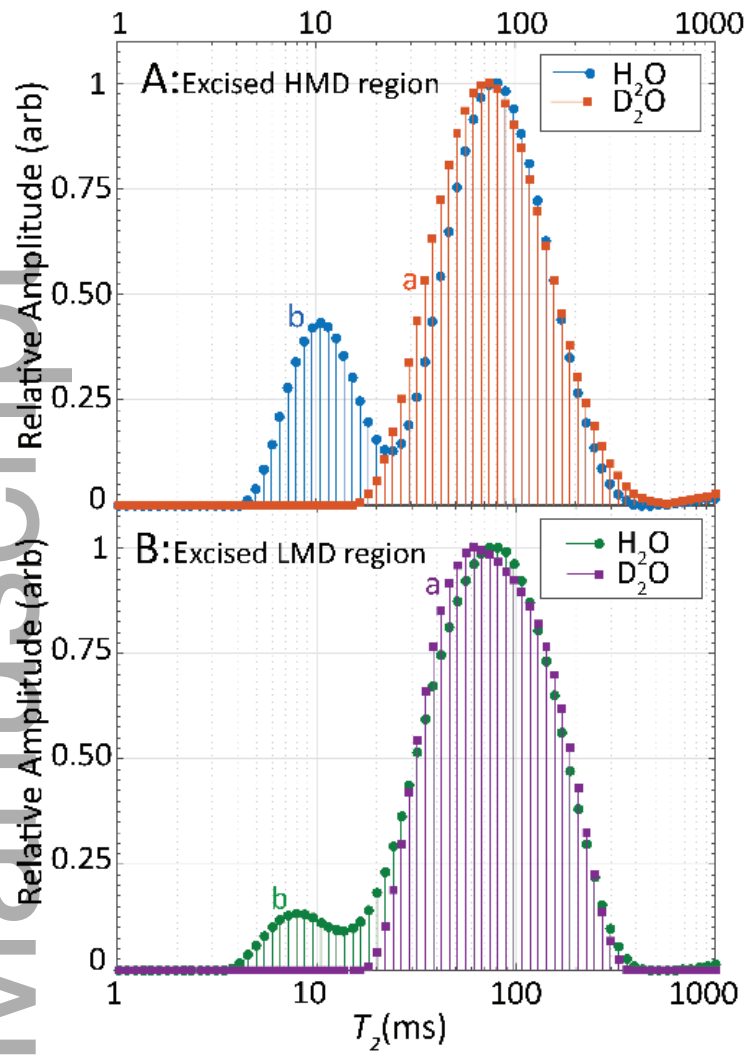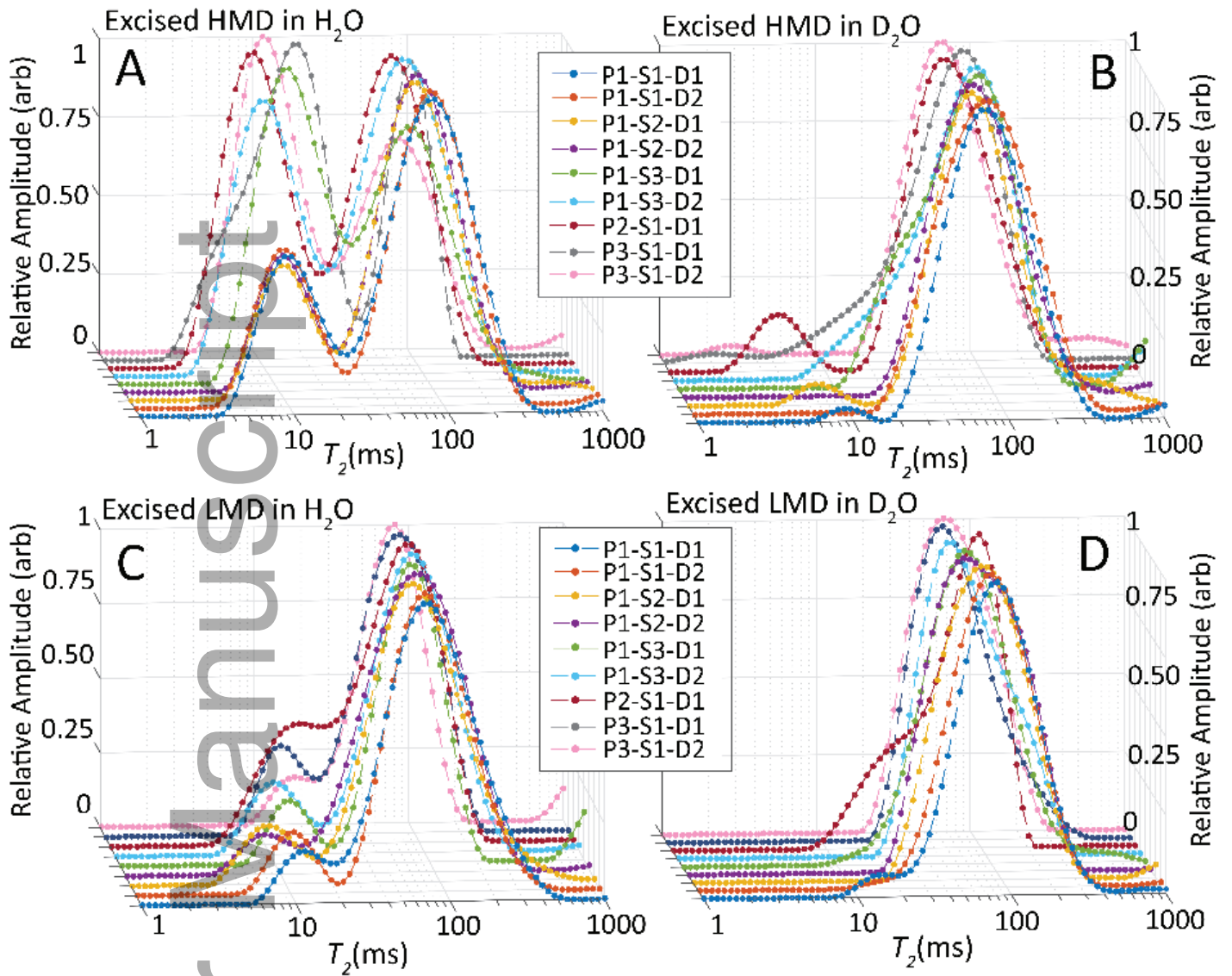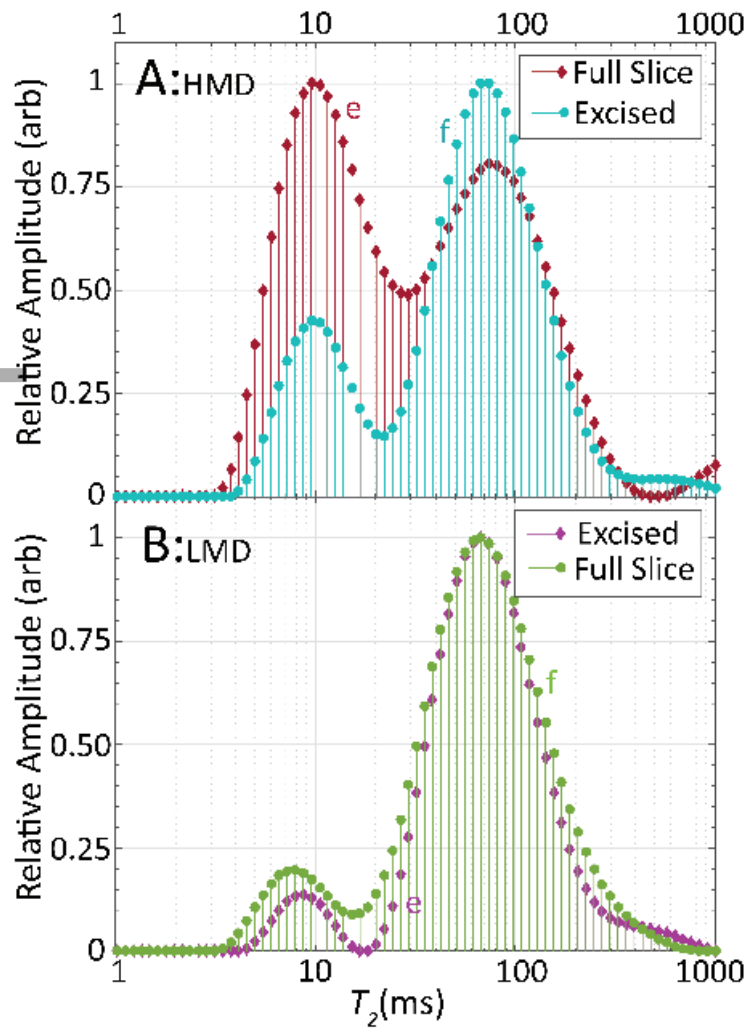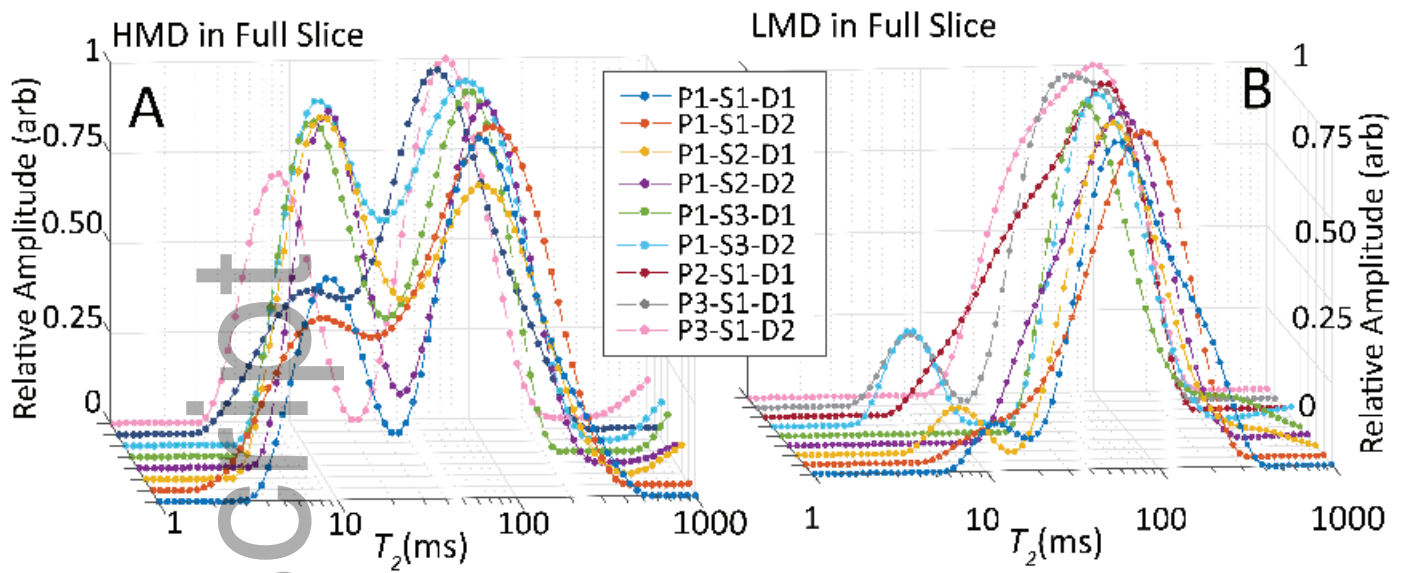
mrm_27781_f1.tif

mrm_27781_f2.tif

mrm_27781_f3.tif

Excised HMD in H₂O — Panel A

Excised HMD in D₂O — Panel B

Excised LMD in H₂O — Panel C

Excised LMD in D₂O — Panel D

Legend (Panels A–B and C–D):
- P1-S1-D1
- P1-S1-D2
- P1-S2-D1
- P1-S2-D2
- P1-S3-D1
- P1-S3-D2
- P2-S1-D1
- P3-S1-D1
- P3-S1-D2

mrm_27781_f4.tif

mrm_27781_f5.tif

HMD in Full Slice

LMD in Full Slice

A

B

Relative Amplitude (arb)

Relative Amplitude (arb)

$T_2$(ms)

$T_2$(ms)

Legend:
- P1-S1-D1
- P1-S1-D2
- P1-S2-D1
- P1-S2-D2
- P1-S3-D1
- P1-S3-D2
- P2-S1-D1
- P3-S1-D1
- P3-S1-D2

mrm_27781_f6.tif

Author Manuscript
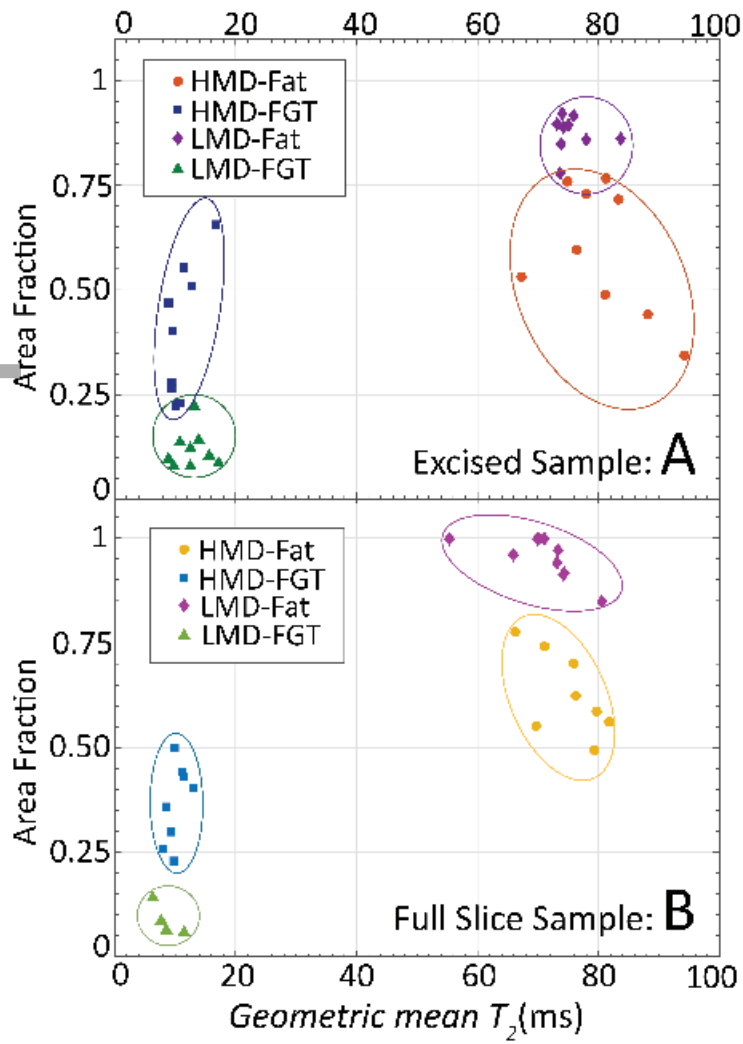
mrm_27781_f7.tif

Author/s:
Ali, TS; Tourell, MC; Hugo, HJ; Pyke, C; Yang, S; Lloyd, T; Thompson, EW; Momot, KI

Title:
Transverse relaxation-based assessment of mammographic density and breast tissue composition by single-sided portable NMR.

Date:
2019-09

Persistent Link:
http://hdl.handle.net/11343/285791

File Description:
Accepted version